Interfacial Insight in Multi-junction Metal Oxide Photoanodes for Water-splitting Applications

A. Mettenbörger,[a] Y. Gönüllü,[a] T. Fischer,[a] T. Heisig,[a] A. Sasinska,[a] C. Maccato,[b] G. Carraro,[b] C. Sada,[c] D. Barreca,[d] L. Mayrhofer,[e] M. Moseler,[e] A. Held,[e] and S. Mathur[a,]

[a] Institute of Inorganic Chemistry, University of Cologne, Greinstr. 6, Cologne D-50859, Germany.

[b] Department of Chemistry, Padova University, and INSTM, via Marzolo 1, 35131 Padova, Italy.

[c] Department of Physics and Astronomy, Padova University, via Marzolo 8, 35131 Padova, Italy.

[d.] CNR-IENI and INSTM, Department of Chemistry, Padova University, via Marzolo 1, 35131 Padova, Italy.

[e] Fraunhofer Institute for Mechanics of Materials (IWM), Freiburg, Germany.

[f] International Research Center for Renewable Energy, School of Energy & Power Engineering, Xian Jiaotong University, Xian (Shaanxi) 710049, PR China.

Abstract

Photoelectrochemical (PEC) performances of nanostructured hematite (Fe_2O_3) thin films prepared using plasma-enhanced chemical vapor deposition (PE-CVD) were investigated against the influence of processing parameters and post-synthesis heat treatment. Annealing at high temperatures was found to substantially affect the surface morphology (FE-SEM) and concomitantly an enhancement in the PEC behavior was observed. The Sn impurity level in hematite films was found to increase with the annealing temperature producing the best synergistic affect, due to the diffusion and substitution of Sn(IV) species at Fe(III) sites, in samples heat-treated at 750°C. Sn:Fe_2O_3 films exhibited significantly high photocurrent density of 1.33 $mAcm^{-2}$ at the water oxidation level of 1.23 V vs. RHE. The diffusion of Sn ions into iron oxide lattice, which altered the electronic properties of hematite films due to electron-donor behavior of the dopants, was verified by detailed X-ray photoelectron spectroscopy and secondary ion mass spectroscopy (SIMS) analyses.. Fabrication of a nanoscopic overlayer of TiO_2 (10 nm) on hematite films by atomic layer deposition was found to further improve the photocurrent density to 1.8 $mAcm^{-2}$ at 1.23 V vs. RHE. Ab-initio calculations were used to investigate the effect of substitutional Sn(IV) dopants in the Fe_2O_3 lattice on the electronic structure and the band alignment between hematite and the TiO_2 over layer. The main findings are that the Sn-dopants lead to the generation of localized Fe(II) centers augmenting the n-type doping of hematite. No effect of the Sn-doping on the electrostatic potential was found on a macroscopic scale. However, the charge transfer from the Sn-dopants to the Fe(II) centers leads to high electric fields on the nanometer scale and might hence play an important role in the efficient separation of electron and holes. The simulations showed that the hematite band edges are enclosed by the TiO_2 band edges. Hence, electron depletion at the surface-liquid interface is enhanced. This might lead to reduced recombination rates near the surface and consequently to increased photocurrents**,** since the Fe_2O_3/TiO_2 interface constitutes a barrier for hole transport

1. Introduction

Photoelectrochemical splitting of water to produce hydrogen is a viable approach to transform sunlight into chemical energy, which has triggered a quest for suitable photocatalysts. Among different semiconductor metal oxides, hematite (α-Fe_2O_3) has emerged as a promising photo-anode material for water oxidation since it is cheap, abundant, non-toxic and stable under photoelectrochemical conditions.[1] Although it promises high theoretical photocurrent densities (11–14 mA/cm^2), corresponding to a solar-to-hydrogen (STH) efficiency of 14-17 %, these values can hardly be attained since hematite suffers from high resistivity,[2] short lifetime of the photoexcited charge carriers,[3, 4] and short hole diffusion length (2-4 nm).[5] Few of these limitations can be overcome by optimizing the nanostructure and electronic properties, as recently shown in a number of studies. For instance, Warren et al.[6] published a work on Si-doped nanostructured hematite electrodes, which gave a photocurrent of approximately 1.70 mA/cm^2 at 1.23 V vs. RHE.

The experimental conditions used for synthesizing α-Fe_2O_3 films directly influence their photoelectrochemical (PEC) behavior. Dendritic α-Fe_2O_3 films prepared by atmospheric pressure-chemical vapor deposition (APCVD) yielded enhanced photocurrents for water oxidation due to the generation of photo-holes at short distances from the semiconductor-electrolyte interface.[7, 8] Wang *et al.*[9] showed that by increasing the post-deposition annealing temperature from 450°C to 750°C, the photocurrent density could be enhanced 2–3 times due to the diffusion of tin ions from the fluorine-doped SnO_2 (FTO) substrates into the hematite structure. An alternative approach to enhance the photoactivity of metal oxide photoanodes is to fabricate heterojunctions by depositing another metal oxide film on top or beneath the original photoanode. This results in optical and electrical modifications of the electrode, improving the charge carrier separation properties.[10] Sharma *et al.*[11] have shown that fabricating a multilayered TiO_2/Fe_2O_3 electrode through sol-gel processes resulted in approximately 10-fold improved photocurrent with respect to the case of a single layer hematite electrode. However, electron transfer between multilayers was found to be poor in samples processed by liquid-phase depositions in comparison to gas phase methods,[12] presumably due to the large number of cracks and pinholes present in solution derived films. As a matter of fact, vapor-phase methods, such as plasma enhanced chemical vapor deposition (PE-CVD) and atomic layer deposition (ALD), enable to minimize surface contamination and challenges of differential grain growth associated with multi-step processing, resulting in an improved control of material characteristics.[13] Among gas phase techniques, ALD offers a unique advantage of atomically modifying the surface properties of the original semiconductor film due to its self-limiting nature that can additionally reduce the surface or lattice defects in proximal layers, producing optimal electronic junctions.[14] Herein, we report a tandem PE-CVD and ALD process developed for Fe_2O_3/TiO_2 multilayer electrodes that exhibit significantly better onset potential (0.8 V *vs* RHE) and high photocurrent density (6 mA/cm^2 at 1.8 V *vs*. RHE), when compared with electrodes having single Fe_2O_3 layer (1 V *vs*. RHE). Moreover, we focus our attention on understanding the PEC behavior of Fe_2O_3-TiO_2 nano-heterostructures through experimental and the theoretical studies have supported the effect of Sn doping and multilayering.

2. Experimental

2.1 Material Synthesis

Hematite thin films were deposited via PE-CVD onto conductive FTO substrates (Sigma Aldrich, ~8Ω/sq) as reported earlier.[13, 15] The substrates were cleaned before deposition by ultarsonication in water and isopropanol followed by Ar plasma etching at 20 W for 3 min. Iron pentacarbonyl [$Fe(CO)_5$] (Acros Organics) was used as the molecular iron precursor. The deposition was performed in a PE-CVD chamber (Domino, Plasma Electronic, Germany), which was pumped down to a base pressure of approximately 0.5 Pa, before the precursor and 20 sccm of O_2 as reactive gas were introduced. After adjusting the pressure to 3.2 Pa, the plasma process was carried out with a Radio Frequency (RF) power of 100 W, resulting in a bias potential of 650 V. The deposition time was varied between 5 and 60 min to optimize the thickness of the hematite thin films. In order to crystallize the amorphous films, the as-deposited specimens were annealed in air at 550°C or 750 °C for 2 h. All electrodes were produced in one batch to guarantee that only the post-deposition treatment differed between the samples.

Deposition of TiO_2 thin films was performed in a commercial BENEQ TFS 200 reactor. $Ti(OiPr)_4$ and water were used as the precursor gases. The temperature of the titanium precursor was kept at 90 °C. Water was constantly cooled down to 20 °C. The hot-wall-reactor temperature was 150 °C. Nitrogen was used as purging gas. The nitrogen flow rates were 300 sccm (chamber flow rate) and 150 sccm (process flow rate).

The pulsing time of $Ti(OiPr)_4$ was 300 ms, followed by a purge of 1 s. Pulsing and purging of water were done each for 500 ms. 170 ALD-cycles were carried out to achieve a film thickness of approximately 10 nm. The as-deposited TiO_2 films were annealed in air at 500 °C for 3 h.

2.2 Materials Characterization

Film morphology was analyzed by FE-SEM using a Zeiss SUPRA 40VP field emission instrument with typical primary beam voltages of 10.0 kV. Optical absorption spectra were measured using a Perkin-Elmer Lambda 950 spectrophotometer, operating in transmittance mode and at normal incidence using a clean FTO substrate as the reference. . Surface XPS spectra were recorded on a Perkin Elmer Φ 5600ci spectrometer at a pressure lower than 10^{-8} mbar, using a non-monochromatized AlKα excitation source ($h\nu$ = 1486.6 eV). The spectrometer was calibrated by assigning the $Au4f_{7/2}$ line to a Binding Energy (BE) of 84.0 eV with respect to the Fermi level. The BE shifts were corrected assigning the C1s line of adventitious carbon to a value of 284.8 eV.[16] The estimated standard deviation for BEs was ±0.2 eV. After a Shirley-type background subtraction,[17] atomic compositions were evaluated using sensitivity factors provided by Φ V5.4A software. Ar ion sputtering was performed at 3.5 kV, with an argon partial pressure of 5×10^{-8} mbar. SIMS measurements were carried out with a IMS 4f mass spectrometer (Cameca) using a 14.5 keV Cs^+ primary beam (current 25 nA, stability 0.2 %) and by negative secondary ion detection, using an electron gun for charge compensation. Depth profiling was carried out rastering over a 150×150 μm^2 area and detecting secondary ions from a sub-region close to 10×10 μm^2 to avoid crater effects. The signals were recorded in beam blanking mode (i.e. interrupting the sputtering process during magnet stabilization periods) in order to improve the in-depth resolution, operating in high-mass resolution configuration to avoid mass interference artefacts. Raman spectra were measured using a Renishaw spectrometer equipped with an Ar laser (λ = 514 nm) excitation source. The film thickness was estimated by DektakXT Profiler (Bruker). The hematite thin films were deposited on silicon substrates by using a mask and the depth profile between substrate and thin films were measured. X-ray diffraction (XRD) patterns were measured (STOE-STADI MP) in glancing incidence (Ω = 2°) mode using Cu Kα (λ = 0.15406 nm) radiation. Electrochemical measurements were performed in a flat three-electrode electrochemical cell using a saturated calomel electrode (SCE) as the reference, a Pt wire as the counter electrode and 1 M NaOH as the electrolyte (pH = 13.6). Linear sweep voltammetry (10 mV/s) was carried out in a potential range from -1 to 1 V vs. SCE using a potentiostat (PAR, Versa state IV) in dark and under simulated solar illumination (Xe lamp, 150 W, Oriel with a Schott KG-3 filter). Potentials with respect to the reversible hydrogen electrode (RHE) scale were calculated using the Nernst equation (1).

$$E_{RHE} = E_{SCE} + E_{SCE}^{0} + 0.059pH \qquad (1)$$

2.3 Simulations

The Vienna ab initio simulations package (VASP) was used for ab initio calculations.[18] In VASP the valence electrons are described by a plane wave basis set and the core electrons are taken into account using the projector-augmented wave formalism.[19, 20] The majority of the simulations were performed within the PBE+U framework.[21] Here, the properties of the strongly correlated d-electrons are corrected by a Hubbard-like term for the onsite Coulomb interactions. Using a value of 5 eV for the Hubbard U and a value of 1 eV for the exchange parameter J, a band gap of 2.1 eV was obtained in excellent agreement with the experimental data. Our choice of U is similar to earlier DFT+U calculations of hematite.[22, 23] For the energy cutoff that defines the plane wave basis set we used a value of 400 eV. In case of the smallest hexagonal unit cell of Fe_2O_3 containing 6 formula units we used a 8×8×4 Monkhorst-Pack grid and a Gaussian smearing with a width of 0.1 eV for the k-point sampling. For larger super cells the k-point sampling was adjusted accordingly. Structural relaxations were performed until all forces were smaller than 0.015 eV/Å. For the alignment of the Fe_2O_3 and TiO_2 band edges we employed the HSE hybrid functional in the HSE06 flavor.[24] However, in the case of Fe_2O_3 only 12% of Hartree-Fock were admixed to the PBE functional, as suggested by Pozun and Henkelman.[25] A 4×4×2 Monkhorst-Pack k-point sampling was used for the hybrid TiO_2 calculation. For the hybrid Fe_2O_3 calculation, a 8×8×4 Monkhorst-Pack grid was used again.

3. Results and Discussion

Iron(III) oxide thin films were deposited on FTO substrates using $Fe(CO)_5$ precursor through a PE-CVD process as previously reported by us.[13, 15] The deposition time and post-deposition annealing procedure had a pronounced effect on the morphology and grain size of films, as evidenced in the FE-SEM micrographs of specimens calcined at 550 °C and 750 °C (Figure 1). Typically, PE-CVD growth yields columnar iron oxide structures, which are favorable for water oxidation applications as they enable faster diffusion of carriers to the charge collector.[6, 13, 15, 26] The sample annealed at 550 °C consist of smaller grains along with the presence of internal voids, whereas annealing at 750°C produced more compact structures driven by grain growth that effectively reduced grain boundaries that can act as electron traps in the samples.[27]

Due to the short diffusion lengths of charge carriers in hematite (approximately 2-4 nm),[28, 29] finding an optimal film thickness that provides minimum recombination rates and maximum light absorption is a critical challenge. In order to determine the film growth rate in the PE-CVD process, iron oxide was grown for different deposition times (5 to 60 min), which gave a growth rate of 61 ± 3 nm/min, as validated by profilometric data (Figure 2).The change in the thickness of the iron oxide films did influence the absorption behavior of the electrodes (Figure 3) by increasing absorption as a function of thickness.

The observed tin diffusion into the hematite films did not form mixed-metal phases as verified by Grazing Incidence X-ray Diffraction (GIXRD) patterns, collected with an incident angle of 2°. For hematite thin film samples annealed at 550 °C and 750 °C for various times (Figure 4a), besides the reflexes at 26.1°, 27.4°, 30.2°, 37.3°, and 50.9°, which can be assigned to the FTO substrate, all samples exhibited pure rhombohedral α-Fe_2O_3 phase with 2Θ values of 24.1°, 33.1°, 35.6°, 40.8°, 49.4°, 57.5° corresponding to the (012), (104), (110), (113), (024), (018) diffraction planes. These finding were confirmed by Raman spectra that revealed the spectral signature Raman modes (231, 250, 298, 414, 506 and 614 cm^{-1}) of hematite (Figure 4b). [32]

XPS analysis of the hematite films heat-treated at 550 °C showed the presence of Fe, O and C (Figure 5a). On the other hand, the specimen annealed at 750°C displayed the occurrence of Sn3d peaks, possibly due to temperature-induced diffusion of Sn dopant ions from the FTO substrate into hematite films.[9] The C1s photoelectron peak main component (BE = 284.8 eV, Figure 5b) can be attributed to adventitious carbon contamination of the samples, whereas the shoulder at BE $\approx$ 288.0 eV could be assigned to the formation of carbonate/hydrocarbons species, likely arising from exposure of samples to ambient air and subsequent adsorption of CO_2 molecules. [16, 30] C signals were eliminated after mild Ar sputtering, indicating that carbon contamination was limited to the sample surface. The O1s signal position (BE = 529.7 eV; compare Figure 5c) agreed to a good extent with lattice oxygen in hematite. The tailing at higher binding energies could be assigned to surface hydroxyl groups, adsorbed O_2 and carbonates.[30, 31] The O/Fe overall atomic ratio was close to 1.5, indicating the formation of stoichiometric Fe_2O_3. Irrespective of the annealing temperature, the Fe2p3/2 peak position (BE =711.0 eV; Figure 5d) and its separation from the Fe2p1/2 component (spin-orbit separation of 13.5 eV) were in good agreement with the presence of iron(III) oxide.[30] No appreciable variations in the position and shape of Fe2p photoelectron peaks were observed between the two specimens. Finally, the Sn3d5/2 peak position (BE = 486.0 eV; Figure 5e) and its separation from the Sn3d3/2 component (9.2 eV) were in good agreement with the presence of Sn(IV) species,[16] as expected for the FTO substrate. The presence of Sn at the surface of the sample annealed at 750 °C (overall amount 0.3 at. %) suggested a thermally induced diffusion of Sn ions from the substrate, since no traces of Sn were detected in the samples annealed at 550°C.

In order to further investigate the occurrence of this phenomenon and to gain information on the in-depth composition of the samples, SIMS depth profile analyses were undertaken. Fe and O ionic yields presented a correlated trend, as expected for the presence of Fe_2O_3 throughout the film thickness. Moreover, the SIMS profiles showed that the samples treated at 750 °C presented a broad interface with the substrate, with an appreciable diffusion of Sn (see Figure 6) into the Fe_2O_3 film, in line with the above observations.

The sample annealed at 550°C for 2 h exhibited a poor PEC response with a high onset potential of 1.10 V *vs*. RHE. Moreover, it had a very low photocurrent density of 0.01 mAcm^{-2} at the water splitting potential of 1.23 V vs. RHE (Figure 7a inset). By increasing the calcination temperature to 750°C for 15 min (Figure 7a), the photoelectrochemical performance increased substantially, with the onset potential shifting to more cathodic value of approximately 0.80 V and the photocurrent density rising to 0.21 mAcm^{-2} at 1.23 V vs. RHE. This change in photocurrent density apparently results from (i) change in surface morphology that decreases the amount of recombination centers on the surface,[6] (ii) diffusion of Sn[9] that can enhance the electron density due to acting as a donor and (iii) reduce the crystallographic mismatch between Fe_2O_3 and FTO, ultimately leading to denser microstructure responsible for faster charger carrier extraction. Increasing the annealing time from 15 to 30 minutes had only a marginal effect on the PEC performance (Fig. 7a).

By further increasing the annealing time to 1 h, the highest photocurrent density of 0.56 mAcm^{-2} at 1.23 V vs. RHE and a maximum photocurrent of 0.82 mAcm^{-2} at 1.60 V vs. RHE was obtained. Although the photoelectrochemical response was drastically improved by annealing the samples at higher temperatures, the photocurrent density of the samples remained low (Figure 7) compared with previous literature. This observation can be attributed to an inadequate film thickness, leading to a high recombination rate or insufficient film absorption.

It is known that the deposition time and therefore the film thickness influence the PEC performance of hematite photoanodes.[13, 32] To determine the influence of film thickness, the photelectrochemical response was measured for iron oxide thin films deposited for different times. The photocurrent onset potential shifts from 0.92 V vs. RHE for the sample deposited for one hour to a more cathodic value of 0.73 V vs. RHE for the sample deposited for 5 min, which is most likely due to the insufficient charge carrier mobility and a high rate of recombination in bulk iron oxide. In addition to the very favorable cathodic shift of photocurrent onset potential, the photocurrent density increases to 1.33 mAcm^{-2} at 1.23 V vs. RHE and a maximum photocurrent of 2.41 mAcm^{-2} at 1.6 V vs. RHE is also obtained.

Simulations within the PBE+U framework were carried out in order to examine the effect of substitutional Sn(IV) dopants on the electronic properties of the hematite host matrix. In agreement with previous simulations using the PBE+U method or hybrid functional[22, 25] we found that undoped hematite is a charge transfer semiconductor with the upper valence band states being mainly formed by O 2p states and the conduction band states are derived from Fe 3d states. The indirect band gap of 2.14 eV obtained by our simulations agrees well the experimental values. As electronic ground state the antiferromagnetic +--+ ordering along the [0001] direction of the hexagonal unit cell was identified. The substitution of a Fe(III) ion by a Sn(IV) ion lead in our calculations to the formation of an occupied localized state 1.11 eV above the valence band edge. This state is generated by the transfer of charge from the Sn(IV) dopant to a neighboring Fe ion, which changes its valence state from +III to +II (Figure 8). This scenario is in qualitative agreement with the hybrid functional calculations in ref. [25], although in the latter work the blue shift of the highest occupied band relative to the valence band maximum is more pronounced and has a value of 1.82 eV. The simulations show that Sn incorporation into the hematite lattice leads to n-type doping and hence to increase charge carrier concentrations and finally to increased conductivity. Moreover, it has been shown theoretically that Sn doping can lead to decreased effective masses of the charge carriers and hence to higher charge carrier mobilities.[33] Since the unfavorable charge transport properties of hematite are considered to be a main reason for high electron-hole recombination rates, an enhancement of the conductivity via doping is a crucial requirement to obtain high photocurrents with hematite photoelectrodes.[34]

In the next step we investigated the possible effects of Sn doping on the electrostatic potential within hematite, in order to clarify whether Sn doping might lead to a favorable downward band bending that drives electrons from the hematite bulk to the FTO substrate and holes in the opposite direction. For these investigations we constructed a 2×2×2 supercell from the hexagonal unit cell containing 240 atoms with a length of 2.77 nm in the [0001] direction (Figure 8a). In the lower half of the supercell we randomly replaced two Fe ions by Sn ions, thus obtaining a doping concentration Sn/(Fe-Sn) of 4.3% in the lower half of the unit cell. In total we generated 40 different random samples and relaxed the corresponding structures. In order to determine the effect of the dopants on a possible potential drop between the doped and the undoped regions we determined the mean electrostatic potential at the cores of the O atoms. By averaging over all 40 samples, a measure for the net effect of doping on the potential profile in the [0001] direction was obtained. As shown in Figure 8b, the averaged effect of Sn-doping on the evolution of electrostatic potential profile is marginal. Taking the average overall core potentials in the doped and undoped region, respectively, we find a negligible potential difference of 0.002 V. Hence, our simulations suggest that Sn-doping has no significant effect on the electrostatic potential landscape on a macroscopic scale. However, the analysis of our simulations showed that the individual samples do exhibit considerable potential changes and hence high electric fields near the Sn dopants. In order to investigate this effect further we examined the electrostatic potential for single Sn dopants in the 2×2×2 supercell. For the investigated cases, we found a potential drop of approximately 0.25 V parallel to the [0001] axis (Figure 8c). The direction in which the potential drop occurs depends on the relative position between the Sn dopant and the adjacent Fe(II) center. The origin of the electrostatic potential gradient is the charge transfer between the Sn(IV) and the Fe(II) ions, which leads to the formation of a local dipole and hence to local electric fields. We propose that these local electric fields might play an important role for the efficient separation of electrons and holes after the photoexcitation in analogy to organic photovoltaic devices, where local potential gradients generated by nanostructured bulk heterojuntions play a decisive role for efficient electron-hole separation.[35, 36] In order to further evaluate the effect of local electric fields due to charge transfer between dopants and the host lattice on charge carrier separation and transport, a more detailed picture of the electrostatic landscape on a larger length scale not directly accessible by ab-initio calculations will have to be constructed. Such a study is beyond the scope of the present article, but might in the future reveal new aspects concerning the effect of doping on the performance of photocatalytic materials.

Since experimental XRD studies showed a slight expansion of the hematite lattice in the $[11\bar{2}0]$ direction due to Sn-doping,[37] we calculated the corresponding deformation potential of hematite following.[38] Consistent results of $\frac{dE}{dln\Omega} = 3.6$ eV were obtained by using the 1s core levels of both Fe and O atoms as reference potentials. Assuming a lattice expansion of 1 % in the $[11\bar{2}0]$ direction in the case of strong doping concentrations this means a shift in the energy levels of only 0.036 eV between the doped and undoped hematite regions due to the deformation potential. Therefore, we exclude any band bending due to lattice expansion as source of enhanced electron-hole separation in Sn doped hematite.

As discussed previously, a fundamental challenge of hematite remains the significant mismatch between its band edge positions and the water reduction/oxidation potentials.[39] Lin *et al.*[14] have reported that with the conduction band edge being more positive than the potential at which H_2O is reduced to H_2, complete water splitting cannot be achieved without applied biases. Introduction of dopants, such as Ti^{4+} electron donors, is reported to increase the conductivity of Fe_2O_3. However, too high dopant concentration can lead to phase segregation and the formation of mixed Fe-Ti phases. Based on these observations, a very thin TiO_2 layer (10 nm) was grown by ALD using $Ti(O^iPr)_4$ as molecular precursor on hematite photoanodes (5 min deposition time, calcined at 750°C for 1 h). The TiO_2 film was amorphous, and X-ray peaks corresponding only to hematite were observed in the TiO_2/Fe_2O_3 bilayer. Figure 9 displays the PEC measurements of TiO_2/Fe_2O_3 heterojunction, which reveals an enhancement in the onset potential after the deposition of the TiO_2 top layer. TiO_2 usually exhibits an onset potential around 0.2–0.3 V vs. RHE. However, the onset potential of the Fe_2O_3/TiO_2 samples was found to be around 0.8 V vs. RHE. On the other hand, the photocurrent density increased sharply to 1.8 mA/cm^2 at 1.23 V vs. RHE. It is likely that the presence of a nanoscopic titanium oxide layer atomically modifies the surface features of the hematite films. In addition, the diffusion of Ti ions in Fe_2O_3 from the top and of Sn ions from the bottom might create a triple junction ($Ti:Fe_2O_3/Fe_2O_3/Sn:Fe_2O_3$) that enhances the overall charge carrier density providing greatly enhanced photocurrent values.

Insufficient lifetimes of the photogenerated holes near the surface due to the fast recombination with conduction band electrons and the trapping of holes in surface states has been identified as one of the main obstacles that impede high photocurrent densities in hematite photoanodes.[1] Stimulating the electron depletion near the surface should therefore lead to reduced recombination rates and prolonged hole lifetimes at the surface, hence increasing photoelectrochemical performance of hematite photoelectrodes.[40] We used ab initio calculations in order to investigate whether the band alignment between the Fe_2O_3 and the TiO_2 overlayer favors fast transport of electrons from the surface to the bulk region. HSE type hybrid functionals were used for these calculations to determine the electronic structure of hematite and anatase TiO_2 due to their generally high accuracy in describing the electronic properties of oxide materials. For TiO_2, the HSE06[24] functional was used, while for Fe_2O_3 the same functional was used with only 12% Hartree-Fock (HSE12%) admixture. The latter functional has turned out to be particularly well suited for the description of hematite.[25]

For the calculation of the relative band off-set between Fe_2O_3 and TiO_2, a non-polar interface within the interface induced gap states (IFIGS) model[41] has been assumed. Furthermore, the intrinsic dipole contribution proportional to the difference in electronegativity of both materials has been neglected.[41] This is justified as the electronegativities of Fe_2O_3 and TiO_2 differ only by 40 meV as judged by the geometric mean of the elemental Pauling electronegativities.[42] The band off-set is then obtained by aligning the charge neutrality levels (CNLs) of the bulk materials (Figure 11). A recent comparative study has demonstrated that this approach predicts band off-sets in heterostructure interfaces rather well.[43]

The CNLs have been calculated from the Kohn-Sham eigenvalues of the hybrid functional calculations by averaging the midgap energy over the first Brillouin zone and the topmost N valence bands and bottommost N conduction bands as described by Schleife et al.[44] We have taken N as the number of primitive cells contained in the simulation cells employed in the DFT calculations (N = 3 for Fe_2O_3 and N = 2 for TiO_2). The k-point mesh for the Brillouin zone sampling has been taken as described above for the hybrid functional calculations. An up to six fold increase in the number of bands N considered for the averaging resulted in only marginal changes in the band alignment. As shown in Figure 11, the anatase TiO_2 band edges enclose the band edges of α-Fe_2O_3. This band alignment favours the fast depletion of electrons from the surface and hence suppresses the recombination with holes in the near surface region. This might be an important ingredient for the good performance of the photoelectrode setup of our work considering the discussion above. Former studies on Fe_2O_3/TiO_2 heterostructures have also observed a more efficient separation of electron-hole pairs.[45, 46] On the other hand, the band alignment also leads to a barrier for hole transport towards the surface and is therefore detrimental to high photocurrents. For this reason we propose that the efficiency of a coated hematite photoelectrode could be improved by employing a material for the over layer where the band alignment not only favors fast electron depletion at the surface but also fast hole transport towards the surface. For example, this could be achieved by the upshift of the valence band edge in TiO_2 which is observed after hydrogen treatment.[47]

4. Conclusions

Nanostructured hematite thin films grown with PE-CVD for photoelectrochemical splitting of water were evidently improved by post-deposition annealing that changed both the morphology and the electronic structure due to the diffusion of tin ions from the substrate into the hematite lattice. It was shown that the film thickness, easily controllable by changing the deposition time, and the post-deposition annealing process have a large influence on the photoelectrochemical performance of hematite thin film photoelectrodes. We found a deposition time of 5 min (160 nm thickness) followed by annealing no shorter than 60 min at 750 °C to be the optimal conditions leading to photoanodes with an onset potential of 0.73 V vs. RHE and a photocurrent of 1.33 mA/cm^2 at the water oxidation potential of 1.23 V vs. RHE. The heating step induced diffusion driven insertion of tin ions from the FTO substrate into the hematite lattice, resulting in a reduced amount of grain boundaries inside the nanostructured hematite columns. Both effects can result in higher charge carrier mobilities through hematite matrices. Furthermore, the best performing photoanodes were covered with a 10 nm thin film of TiO_2 by ALD. The ab initio calculations showed that the Sn dopants lead to the generation of localized Fe(II) centers, conforming with an n-type doping of hematite. However, the charge transfer from the Sn dopants to the Fe(II) centers leads to high electric fields on the nanometer scale and might hence play an important role in the efficient charge carrier separation. The simulations show that the hematite band edges are enclosed by the TiO_2 band edges. Hence electron depletion at the surface liquid interface is enhanced.

Acknowledgements

The authors kindly acknowledge the financial support under the FP7 project “SOLAROGENIX” (NMP4-SL-2012-310333), as well as from the University of Cologne, Germany.The support by Padova University ex-60% 2012-2013 projects, PRAT 2010 (n° CPDA102579) and Regione Lombardia-INSTM ATLANTE projects is also acknowledged. Funding from the New Indigo Partnership Programme (InSOL project) is gratefully acknowledged

Notes and references

Reference:

[1] K. Sivula, F. Le Formal, M. Grätzel, ChemSusChem, 4 (2011) 432-449.
[2] B.M. Klahr, T.W. Hamann, J. Phys. Chem. C, 115 (2011) 8393-8399.
[3] N.J. Cherepy, D.B. Liston, J.A. Lovejoy, H. Deng, J.Z. Zhang, J. Phys. Chem. B, 102 (1998) 770-776.
[4] A.G. Joly, J.R. Williams, S.A. Chambers, G. Xiong, W.P. Hess, D.M. Laman, J. Appl. Phys., 99 (2006) 053521-053526.
[5] K. Sivula, F. Le Formal, M. Grätzel, ChemSusChem, 4 (2011) 432-449.
[6] S.C. Warren, K. Voïtchovsky, H. Dotan, C.M. Leroy, M. Cornuz, F. Stellacci, C. Hébert, A. Rothschild, M. Grätzel, Nat. Mater., (2013) 842-849.
[7] A. Kay, I. Cesar, M. Grätzel, J. Am. Chem. Soc., 128 (2006) 15714-15721.
[8] Y. Ling, G. Wang, D.A. Wheeler, J.Z. Zhang, Y. Li, Nano Lett., 11 (2011) 2119-2125.
[9] L. Wang, C.-Y. Lee, P. Schmuki, Electrochim. Acta, 91 (2013) 307-313.
[10] S. Choudhary, S. Upadhyay, P. Kumar, N. Singh, V.R. Satsangi, R. Shrivastav, S. Dass, International Journal of Hydrogen Energy, 37 (2012) 18713-18730.
[11] P. Sharma, P. Kumar, A. Solanki, R. Shrivastav, S. Dass, V. Satsangi, J. Solid State Electrochem., 16 (2012) 1305-1312.
[12] M. Liu, M.B. Johnston, H.J. Snaith, Nature, 501 (2013) 395-398.
[13] A.P. Singh, A. Mettenbörger, P. Golus, S. Mathur, International Journal of Hydrogen Energy, 37 (2012) 13983-13988.
[14] Y. Lin, Y. Xu, M.T. Mayer, Z.I. Simpson, G. McMahon, S. Zhou, D. Wang, J. Am. Chem. Soc., 134 (2012) 5508-5511.
[15] A. Mettenbörger, T. Singh, A.P. Singh, T.T. Järvi, M. Moseler, M. Valldor, S. Mathur, International Journal of Hydrogen Energy, 39 (2014) 4828-4835.
[16] J.F. Moulder, W.F. Stickle, P.E. Sobol, K.D. Bomben, Handbook of X-ray photoelectron spectroscopy, Perkin Elmer Eden Prairie, MN1992.
[17] J.E. Castle, Surface and Interface Analysis, 6 (1983) 302-302.
[18] G. Kresse, J. Furthmüller, Phys. Rev. B, 54 (1996) 11169-11186.
[19] G. Kresse, D. Joubert, Phys. Rev. B, 59 (1999) 1758-1775.
[20] P.E. Blöchl, Phys. Rev. B, 50 (1994) 17953-17979.
[21] S.L. Dudarev, G.A. Botton, S.Y. Savrasov, C.J. Humphreys, A.P. Sutton, Phys. Rev. B, 57 (1998) 1505-1509.
[22] G. Rollmann, A. Rohrbach, P. Entel, J. Hafner, Phys. Rev. B, 69 (2004) 165107.
[23] A. Kleiman-Shwarsctein, M.N. Huda, A. Walsh, Y. Yan, G.D. Stucky, Y.-S. Hu, M.M. Al-Jassim, E.W. McFarland, Chem. Mater., 22 (2009) 510-517.
[24] A.V. Krukau, O.A. Vydrov, A.F. Izmaylov, G.E. Scuseria, The Journal of Chemical Physics, 125 (2006) 224106.
[25] Z.D. Pozun, G. Henkelman, The Journal of Chemical Physics, 134 (2011) 224706.

[26] D. Barreca, G. Carraro, A. Gasparotto, C. Maccato, C. Sada, A.P. Singh, S. Mathur, A. Mettenbörger, E. Bontempi, L.E. Depero, Int. J. Hydrogen Energy, 38 (2013) 14189-14199.
[27] B.D. Chernomordik, H.B. Russell, U. Cvelbar, J.B. Jasinski, V. Kumar, T. Deutsch, M.K. Sunkara, Nanotechnology, 23 (2012) 194009.
[28] R.F.G. Gardner, F. Sweett, D.W. Tanner, J. Phys. Chem. Solids, 24 (1963) 1183-1196.
[29] M.P. Dare-Edwards, J.B. Goodenough, A. Hamnett, P.R. Trevellick, Journal of the Chemical Society, Faraday Transactions 1: Physical Chemistry in Condensed Phases, 79 (1983) 2027.
[30] G. Carraro, A. Gasparotto, C. Maccato, D. Barreca, Surf. Sci. Spectra, 20 (2013) 9-16.
[31] G. Carraro, A. Gasparotto, C. Maccato, E. Bontempi, O.I. Lebedev, S. Turner, C. Sada, L.E. Depero, G. Van Tendeloo, D. Barreca, RSC Adv., 3 (2013) 23762-23768.
[32] I. Cesar, K. Sivula, A. Kay, R. Zboril, M. Grätzel, J. Phys. Chem. C, 113 (2009) 772-782.
[33] X. Meng, G. Qin, W.A. Goddard, S. Li, H. Pan, X. Wen, Y. Qin, L. Zuo, J. Phys. Chem. C, 117 (2013) 3779-3784.
[34] Y. Ling, Y. Li, Particle & Particle Systems Characterization, 31 (2014) 1113-1121.
[35] G. Yu, J. Gao, J.C. Hummelen, F. Wudl, A.J. Heeger, Science, 270 (1995) 1789-1791.
[36] G. Yu, A.J. Heeger, J. Appl. Phys., 78 (1995) 4510-4515.
[37] N.T. Hahn, C.B. Mullins, Chem. Mater., 22 (2010) 6474-6482.
[38] C.G. Van de Walle, R.M. Martin, Physical Review Letters, 62 (1989) 2028-2031.
[39] J. Brillet, M. Cornuz, F.L. Formal, J.-H. Yum, M. Grätzel, K. Sivula, J. Mater. Res., 25 (2010) 17-24.
[40] S.R. Pendlebury, X. Wang, F. Le Formal, M. Cornuz, A. Kafizas, S.D. Tilley, M. Grätzel, J.R. Durrant, J. Am. Chem. Soc., 136 (2014) 9854-9857.
[41] W. Mönch, Electronic Properties of Semiconductor Interfaces, Springer Verlag, Berlin

Heidelberg, 2004.
[42] W. Mönch, Semiconductor Surfaces and Interfaces, Springer Verlag, Berlin Heidelberg, 2001.
[43] Y. Hinuma, A. Grüneis, G. Kresse, F. Oba, Phys. Rev. B, 90 (2014) 155405.
[44] A. Schleife, F. Fuchs, C. Rödl, J. Furthmüller, F. Bechstedt, Appl. Phys. Lett., 94 (2009) 012104.
[45] W.-H. Hung, T.-M. Chien, C.-M. Tseng, J. Phys. Chem. C, 118 (2014) 12676-12681.
[46] S. Kuang, L. Yang, S. Luo, Q. Cai, Appl. Surf. Sci., 255 (2009) 7385-7388.
[47] X. Chen, L. Liu, P.Y. Yu, S.S. Mao, Science, 331 (2011) 746-750.
[48] S. Saremi-Yarahmadi, K.G.U. Wijayantha, A.A. Tahir, B. Vaidhyanathan, J. Phys. Chem. C, 113 (2009) 4768-4778.
[49] I. Cesar, A. Kay, J.A. Gonzalez Martinez, M. Grätzel, J. Am. Chem. Soc., 128 (2006) 4582-4583.
[50] S.D. Tilley, M. Cornuz, K. Sivula, M. Grätzel, Angew. Chem., Int. Ed., 49 (2010) 6405-6408.
[51] Y.-S. Hu, A. Kleiman-Shwarsctein, G.D. Stucky, E.W. McFarland, Chem. Commun., (2009) 2652-2654.
[52] S. Shen, C.X. Kronawitter, D.A. Wheeler, P. Guo, S.A. Lindley, J. Jiang, J.Z. Zhang, L. Guo, S.S. Mao, J. Mater. Chem. A, 1 (2013) 14498-14506.
[53] P. Zhang, A. Kleiman-Shwarsctein, Y.-S. Hu, J. Lefton, S. Sharma, A.J. Forman, E. McFarland, Energ. Environ. Sci., 4 (2011) 1020-1028.

[54] G. Wang, Y. Ling, D.A. Wheeler, K.E.N. George, K. Horsley, C. Heske, J.Z. Zhang, Y. Li, Nano Lett., 11 (2011) 3503-3509.
[55] J. Deng, J. Zhong, A. Pu, D. Zhang, M. Li, X. Sun, S.-T. Lee, J. Appl. Phys., 112 (2012) 0843121-0843127.
[56] O. Zandi, B.M. Klahr, T.W. Hamann, Energ. Environ. Sci., 6 (2013) 634-642.
[57] J.A. Glasscock, P.R.F. Barnes, I.C. Plumb, N. Savvides, J. Phys. Chem. C, 111 (2007) 16477-16488.
[58] C.D. Bohn, A.K. Agrawal, E.C. Walter, M.D. Vaudin, A.A. Herzing, P.M. Haney, A.A. Talin, V.A. Szalai, J. Phys. Chem. C, 116 (2012) 15290-15296.
[59] Y.Q. Cong, M.M. Chen, T. Xu, Y. Zhang, Q. Wang, Appl. Catal. B-Environ., 147 (2014) 733-740.
[60] Ingler, J.P. Baltrus, S.U.M. Khan, J. Am. Chem. Soc., 126 (2004) 10238-10239.
[61] S. Kumari, C. Tripathi, A.P. Singh, D. Chauhan, R. Shrivastav, S. Dass, V.R. Satsangi, Curr. Sci., 91 (2006) 1062-1064.
[62] V.R. Satsangi, S. Kumari, A.P. Singh, R. Shrivastav, S. Dass, Int. J. Hydrogen Energy, 33 (2008) 312-318.
[63] W.B. Ingler Jr., S.U.M. Khan, Int. J. Hydrogen Energy, 30 (2005) 821-827.
[64] W.B. Ingler Jr., S.U.M. Khan, Thin Solid Films, 461 (2004) 301-308.
[65] A. Kleiman-Shwarsctein, Y.-S. Hu, A.J. Forman, G.D. Stucky, E.W. McFarland, J. Phys. Chem. C, 112 (2008) 15900-15907.
[66] Y.-S. Hu, A. Kleiman-Shwarsctein, A.J. Forman, D. Hazen, J.-N. Park, E.W. McFarland, Chem. Mater., 20 (2008) 3803-3805.
[67] H.G. Cha, J. Song, H.S. Kim, W. Shin, K.B. Yoon, Y.S. Kang, Chem. Commun., 47 (2011) 2441-2443.
[68] C. Sanchez, K.D. Sieber, G.A. Somorjai, J. Electroanal. Chem., 252 (1988) 269-290.
[69] P. Kumar, P. Sharma, R. Shrivastav, S. Dass, V.R. Satsangi, Int. J. Hydrogen Energy, 36 (2011) 2777-2784.
[70] L. Wang, C.-Y. Lee, P. Schmuki, Electrochem. Commun., 30 (2013) 21-25.
[71] X. Zhang, H. Li, S. Wang, F.-R.F. Fan, A.J. Bard, J. Phys. Chem. C, 118 (2014) 16842–16850.
[72] Y. Liu, Y.-X. Yu, W.-D. Zhang, Electrochim. Acta, 59 (2012) 121-127.

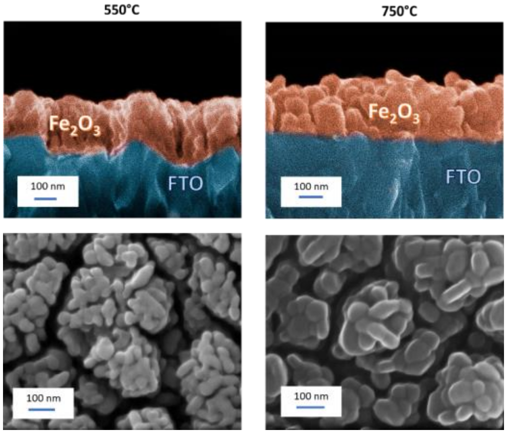

Figure 1: Cross-sectional and plane- view FE-SEM micrographs of iron oxide thin films deposited via PE-CVD and annealed at 550 and 750 °C for 2 hours.

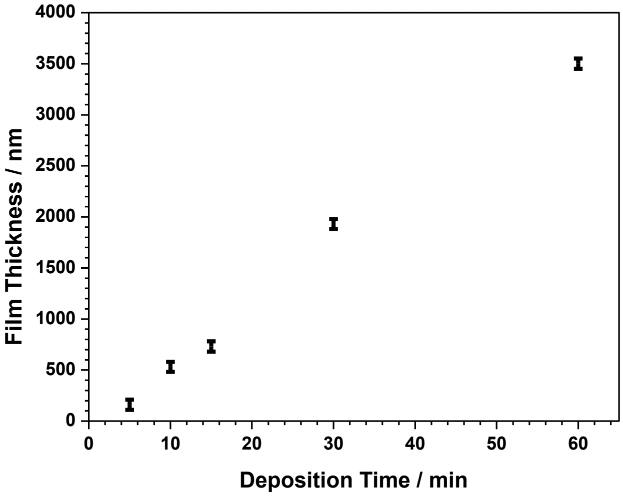

Figure 2: Film thickness of iron oxide films in the PE-CVD process plotted against the deposition time.

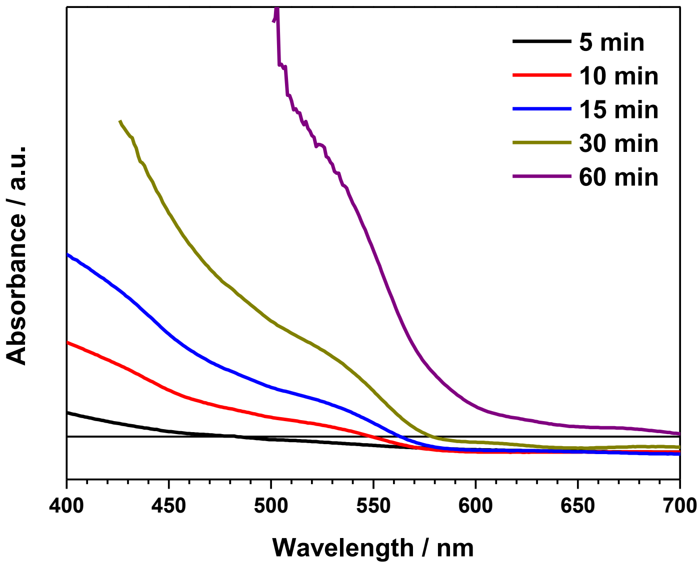

Figure 3: Absorption spectra of PE-CVD grown iron oxide thin films for different deposition times.

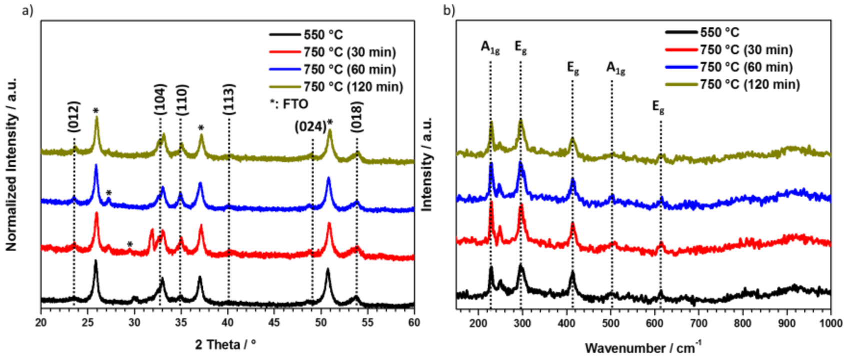

Figure 4: (a) XRD patterns and (b) Raman spectra of iron oxide thin films annealed at 550 °C (for 2h) and 750 °C .

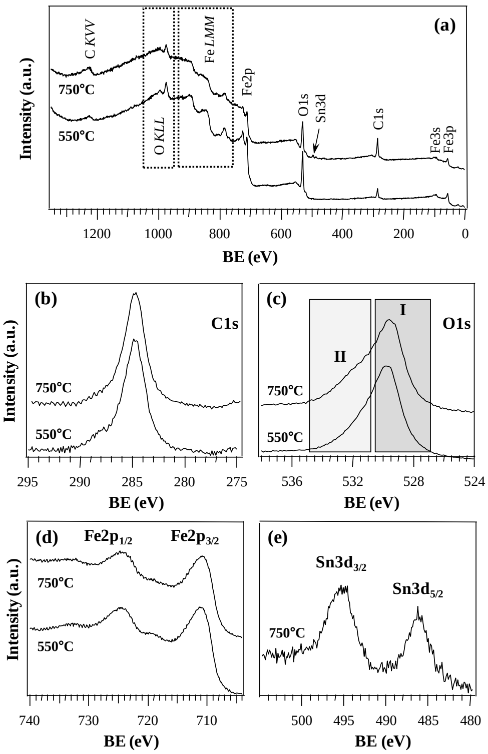

Figure 5: (a) Surface wide-scan XPS spectra for iron oxide samples annealed at 550°C and 750°C for 2h. The detailed (b) C1s, (c) O1s, (d) Fe2p and (e) Sn3d regions are also displayed.

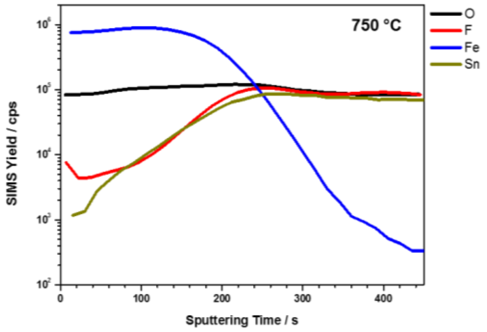

Figure 6: SIMS of iron oxide samples annealed at 750 °C (1h).

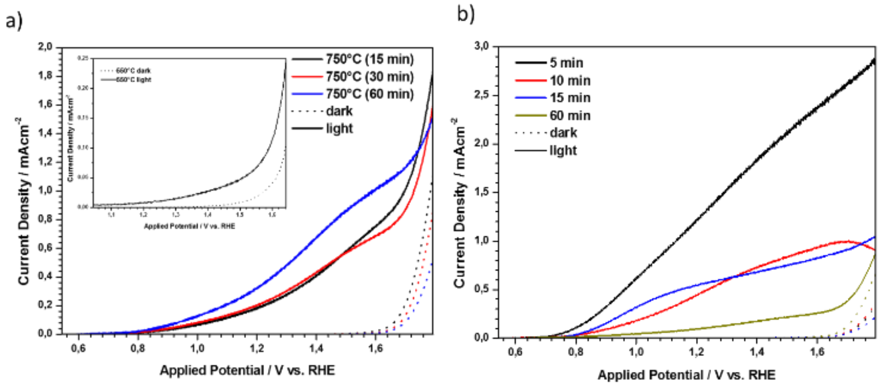

Figure 7: (a) Photocurrent densities of Fe_2O_3 photoanodes deposited for 15 min and annealed at various temperatures and (b) different deposition times as a function of applied potential (annealed at 750°C).

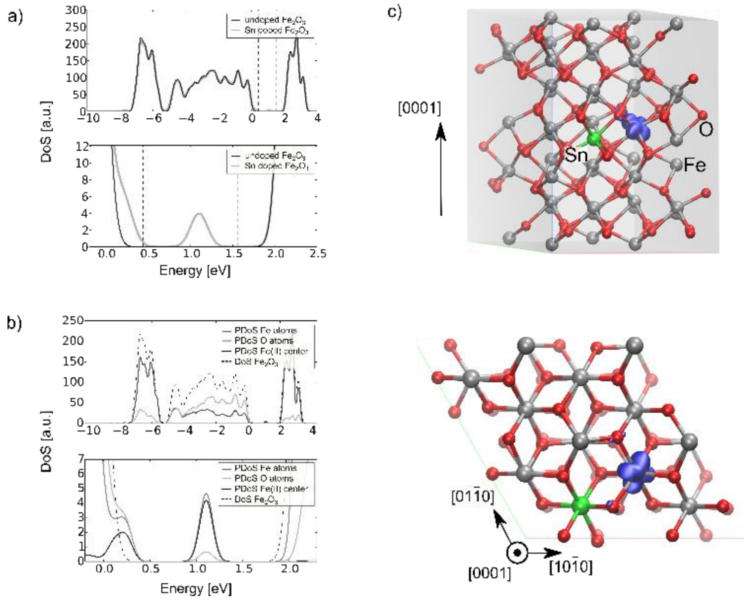

Figure 8: a) Density of states (DoS) for undoped and Sn doped hematite. Sn doping leads to the formation of an occupied midgap state. The Fermi energy is considerably upshifted by the Sn doping as indicated by the vertical dashed lines. b) Density of states of Sn doped hematite projected on the Fe ions, the localized Fe(II) center and the O ions. The projection on the Sn

ion is negligible in the band gap region. In all plots the highest occupied state of the undoped hematite has been used as zero energy reference. c) 2x2x1 supercell of hematite with a single substitutional Sn dopant. In blue an isosurface of the charge density associated with the occupied midgap state is shown. The electron transferred by the Sn(IV) to an adjacent Fe(II) center is strongly localized

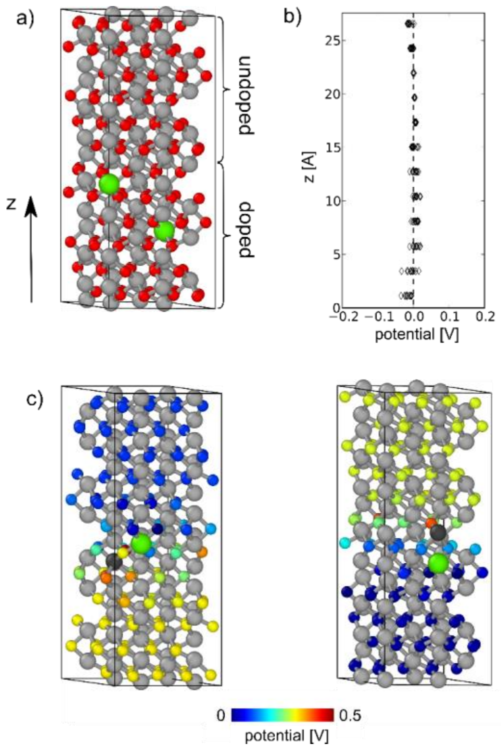

Figure 9: (a) One of the 40 configurations of hematite (Fe grey, oxygen red) with two Sn dopants (Sn green) in the lower unit cell half. (b) Core potentials of the O ions averaged over all 40 random configurations. (c) Two example configurations of single Sn dopants in the 2x2x2 hematite supercell. The oxygen ions are colored according to their core potentials. The Fe(II) center is shown in dark.

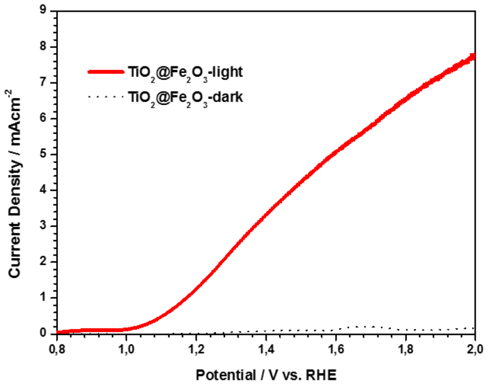

Figure 10: Photoelectrochemical response of Fe_2O_3 photo anodes (5min, 750 °C, 1h) coated with 10 nm TiO_2 as a function of applied potential.

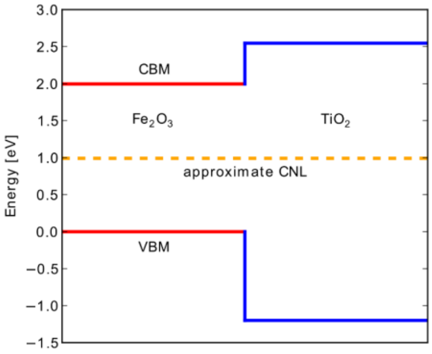

Figure 11: Band alignment between α-Fe_2O_3 and anatase TiO_2 as obtained by aligning the energy scales of both materials at their charge neutrality levels (CNLs). The valence band maximum (VBM) as well as the conduction band minimum (VBM) is plotted for both semiconductors. The origin of the energy scale has been taken as the VBM of α-Fe_2O_3.

Table 1: Comparison of film thickness, onset potential (E_{Onset}) and the photocurrent density (I_{Ph}) at an anodic potential of 1.23 and 1.6 V vs. RHE depending on the deposition time (t) and the calcination temperature (T).

t [min]	**T [°C]**	**d [nm]±50 nm**	**E_{Onset} [V vs. RHE]±0.01V**	**I_{Ph}(1,23 V vs. RHE) [mA/cm^2]±0.01mA**	**I_{Ph}(1,6 V vs. RHE) [mA/cm^2] ±0.01mA**
5	750 (60 min)	160	0.73	1.33	2.41
10	750 (60 min)	530	0.83	0.48	0.93
15	550 (240 min)	530	1.10	0.01	0.07
15	750 (15 min)	530	0.81	0.21	1.00
15	750 (30 min)	530	0.80	0.24	0.69
15	750 (60 min)	530	0.83	0.56	0.82
30	750 (60 min)	1930	-	-	-
60	750 (60 min)	3500	0.92	0.09	0.25

Commentato [G1]: in order to avoid further troubles, we suggest to modify the table, leaving only the refs in NaOH solutions.

In addition, we can convert all the potential in RHE scale.

Table 2: Photoelectrochemical performance of cation doped iron oxide photoelctrodes with respect to the applied potential an electrolyte used.

Dopant	**Photocurrent-density [mAcm^{-2}]**	**Potential**	**Electrolyte**	**Ref.**
Si	2.05	1.23 V vs. RHE	1 M NaOH	[7]
Si	1.67	1.23 V vs. RHE	1 M NaOH	[48]
Si	2.3	1.4 V vs. RHE	1 M NaOH	[32]
Si	1.45	1.23 V vs. RHE	1 M NaOH	[49]
Si	4	1.53 V vs. RHE	1 M NaOH	[6]
Si	3.3	1.23 V vs. RHE	1 M NaOH	[50]
Ti	1.5	0.3 V vs. Ag/AgCl	1 M NaOH	[51]
Ti	0.6	1V vs. Ag/AgCl	0.5 M NaCl	[52]
Ti	1.2	0.6 vs. Ag/AgCl	1 M NaOH	[53]
Ti	1.83	1.02 vs. RHE	1 M NaOH	[54]
Ti	1.91	1.23 vs. RHE	1 M NaOH	[55]
Ti	0.8	1.8 V vs. RHE	0.2 M KCl	[56]
Ti	0.6	1.4 V vs. RHE	1 M KOH	[37]
Ti	0.3	0.3 V vs. SCE	1 M NaOH	[57]
Sn	0.4	1.4 V vs. RHE	1 M KOH	[37]
Sn	1.86	1.23 V vs. RHE	1 M NaOH	[8]
Sn	0.87	1.23 V vs. RHE	1 M KOH	[9]
Sn	2.1	1.6 V vs. RHE	1 M NaOH	[58]
Al	1.1	0.3 V vs. Ag/AgCl	1 M NaOH	[23]
Al	-0.3	0.3 V vs. Ag/AgCl	0.1 M Na_2SO_4 + 0.1 M Na_2SO_3	[59]

Al/Ta	-0.85	0.3 V vs. Ag/AgCl	0.1 M Na_2SO_4 + 0.1 M Na_2SO_3	[59]
Zn (p-type)	1.1	-0.8 (2 Elektroden)	0.5 H_2SO_4	[60]
Zn (n-type)	0.3	0.55 V vs. SCE	1 M NaOH	[61]
Zn (n-type)	0.42	0.6 V vs. SCE	1 M NaOH	[62]
Cu	0.07	0.6 V vs. SCE	1 M NaOH	[62]
Cu (p-type)	0.94	0 V vs. SCE	0.5 H_2SO_4	[63]
Mg (p-type)	-0.4	0.55 V vs. RHE	1 M KOH+0.5M H_2O_2	[14]
Mg (p-type)	0.22	0.2 V vs. SCE	0.5 M H_2SO_4	[64]
Cr	0.7	0.3 V vs. Ag/AgCl	1 M NaOH	[65]
Mo	1.5	0.3 V vs. Ag/AgCl	1 M NaOH	[65]
Pt	1.43	0.4 vs. Ag/AgCl	1 M NaOH	[66]
Pt	1.38	0.23 V vs. Ag/AgCl	1 M KOH	[67]
Nb	0.65	0.5 V vs. SCE	1 M NaOH	[68]
Zr	2.1	0.6 V vs. SCE	1 M NaOH	[69]
Ti/Sn	1.4	1.23 V vs. RHE	1 M KOH	[70]
Ta	-0.85	0.6 V vs. Ag/AgCl	0.1 M Na_2SO_3+ 0.1 M Na_2SO_4	[71]
Ni	1.5	0.65 V vs. Ag/AgCl	1 M NaOH	[72]